PHOTONICS Research

General strategy for ultrabroadband and wide-angle absorbers via multidimensional design of functional motifs

Qi Yuan,[1,†] ![ORCID] Cuilian Xu,[1,†] Jinming Jiang,[1,*] Yongfeng Li,[1,2] Yang Cheng,[1] ![ORCID] He Wang,[1] ![ORCID] Mingbao Yan,[1] Jiafu Wang,[1] Hua Ma,[1] and Shaobo Qu[1]

[1]Department of Basic Science, Air Force Engineering University, Xi'an 710051, China
[2]e-mail: liyf217130@126.com
*Corresponding author: 88jiangjinming@163.com

Developing wide-angle, polarization-independent, and effective electromagnetic absorbers that endow devices with versatile characteristics in solar, terahertz, and microwave regimes is highly desired, yet it is still facing a theoretical challenge. Herein, a general and straightforward strategy is proposed to surmount the impedance mismatching in the ultrabroadband and wide-angle absorber design. A vertical atom sticking on $N \times N$ horizontal meta-atoms with conductive film is proposed as the functional motif, exhibiting the strong ohmic dissipation along both vertical and horizontal directions. Assisted by the intelligent optimization strategy, the structure dimension, location, and film distribution are designed to maintain absorbing performance under different incident angles. As a demonstration, an absorber was designed and proved in both simulation and experiment. Significantly, the over 10 dB absorption from 5 to 34 GHz is achieved in the range of 0° to 70° for both TE and TM, and even 3 to 40 GHz from 60° to 70° for the TE wave. Meanwhile, the proposed multidimensional design of functional motifs can be attached with optical transparency function at will. That is to say, our effort provides an effective scheme for expanding matching area and may also be made in optical, infrared, and terahertz regimes.   © 2022 Chinese Laser Press

https://doi.org/10.1364/PRJ.467612

1. INTRODUCTION

Absorbing electromagnetic (EM) waves in arbitrary directions and polarization has been desired for energy conversion [1–3], EM shielding [4,5], and stealth [6,7] devices in both academia and engineering. By matching the impedance between materials and free space, EM waves can enter materials and then be transformed into other energy [8,9]. There are two typical approaches to design EM absorbers: loss material-based absorbers and structural-based absorbers. Commonly, the loss materials are divided into three types: resistance loss absorption, dielectric loss absorption, and magnetic dielectric loss absorption, which have been utilized to serve the effective absorption in optical, infrared, terahertz and microwave areas [10–22]. While suffering from bulky size, high density, narrowband, or weak resonance, the further development of absorber design is restricted by materials' inherent drawbacks, especially in broadband and wide angles. As an alternative, the structural resonance-based method is introduced, which achieves the electric or magnetic resonance by meticulous arrangement of the dielectric and metal structure. Particularly, the appearance of metamaterials [23–25], consisting of periodic or quasi-periodic

functional motifs, solves the bulky size of the traditional devices and achieves stronger resonance in designed frequency simultaneously, pushing the rapid development EM manipulation as anomalous reflection/deflection [26–28], beam splitting [29–34], RCS reduction [35–38], and holography and imaging [39–44]. Hence, metamaterials have been widely integrated into the study of EM absorbers.

In 2008, Landy *et al.* proposed an I-shaped based method to realize perfect absorption at a single frequency point [45], arousing interest in the metamaterials absorber. This novel resonant mechanism has been promoted to realize the dual-frequency, multiple frequency, and even wideband absorbers [46–52]. Meanwhile, the composite design methods, frequency selective surface (FSS), and plasmonic structure, have been utilized in metamaterials absorbers to expand the operating bandwidth [53–57]. Heretofore, plenty of existing schemes use broadband effective absorption for normal and small incident angles. However, with an increase of the incident angle, the performance of absorbers will decline, especially for TE polarization waves. This kind of impedance mismatching means that ultrabroadband and wide-angle absorbers rarely coexist, i.e., the

so-called property trade-off paradox. As a universal law of nature, such a phenomenon exists widely in the important properties of structural and functional materials. Given that the properties of materials are determined by their structures, the key to realizing the rational design of materials with the desired performance is to dissect the detailed information about the material structures. Recently, achievement of the function-oriented design of new functional materials was developed under the design of functional motifs [58,59], and metamaterials are one of the classical EM functional materials. Thus, it is very necessary to initiate multidimensional design of functional motifs for ultrabroadband and wide-angle absorbers.

In recent years, intelligent optimization algorithms unveiled the curtain of inverse structure's design. By endowing codes with corresponding structural parameters, the dimension, size, distribution, and shape of the functional motifs can be encoded into a mathematical expression or computer language. Following the guidance of the preset goal orientation, the performance of designed functional motifs will exceed that of empirical intuition. Till now, the optimization method has achieved perfect performance in broadband absorption [60–64], polarization conversion [65–67], precise wavefront manipulation [68–70], and so on. However, these reported performances would decline sharply with an increase of the incident angle of EM waves. And the mechanism in these works cannot surmount the impedance mismatch problem in broadband and wide angle. Recently, some spatially combined structures have been proposed to improve the angular tolerance of absorption [71,72], yet the research on this issue is still in the nascent stage.

In this work, a general and straightforward strategy is proposed for ultrabroadband and wide-angle absorbers. Theoretically, a spatial combined manner is derived from the analysis of EM wave vectors, reacting to the large and small incident angle by the top and bottom absorbing structure, respectively. Then, a vertical atom sticking on $N \times N$ horizontal meta-atoms with conductive film serves as the functional motif. Based on centrosymmetric characteristics, the proposed functional motifs were polarization-independent. Meanwhile, the structural parameters were optimized by the intelligent algorithm to satisfy the wide-angle effective absorption. As a proof of concept, a wide-range broadband microwave absorber was fabricated by resistive sheet and dielectric means. This absorber achieves over 10 dB absorption from 5 to 34 GHz in the range of 0° to 70° for both TE and TM waves and 3 to 40 GHz from 60° to 70° for the TE wave. The measured result is highly coincident with the simulated result, verifying the feasibility of our proposed method. Moreover, the proposed functional motifs can be attached with optical transparency function at will. When the resistive sheet was the transparent material indium tin oxide (ITO) and the dielectric was polymethyl methacrylate (PMMA), the transmittance of the ultrabroadband and wide-angle absorbers is maintained over 70% in optical regimes. Thus, it is believed that this multidimensional design manner of functional motifs can be expanded to optical, infrared, and terahertz absorption, and even to multispectral compatible applications.

2. PRINCIPLE AND DESIGN

Figure 1 illustrates the performance of a wide-angle absorber under different EM waves. The proposed functional motifs consist of a vertical atom on $N \times N$ horizontal meta-atoms, which endows the absorber with wide-angle microwave absorption and optical transparency. Under the illumination of microwave, the proposed absorber expresses over 90% absorption for both TE and TM waves in wideband and wide angle, while under the illumination of light waves, the proposed device expresses over 70% transmission. In terms of equivalent circuit parameters, Z_0 is the characteristic impedance of air. $Z_R(\theta)$ and Z_d denote the equivalent impedance of the resistive sheet under different incidences and the dielectric substrate, respectively. In sharp contrast to the traditional absorbing metamaterials, the proposed functional motifs can provide equivalent impedance in both vertical and horizontal directions, which will surmount the impedance-matching problem under wide-angle incident waves.

Figure 2 illustrates the vector decomposition of incident waves. First, we define the direction of normally incident wave as the z axis. For the TE wave, the electric (E)-field is on the y axis for both components k_z and k_x. Perpendicular to the direction of E-field and k, the magnetic (H)-field is along the x axis for k_z and z axis for k_x, respectively. Similarly, for the TM wave, the H-field is on the y axis for both components k_z and k_x. Perpendicular to the direction of H-field and k, the E-field is along the x axis for k_z and along the z axis for k_x, respectively. According to the impedance calculation formula, the impedance under different polarizations can be calculated as

$$Z_{R,\mathrm{TE}}(\theta) = \frac{Z_R}{\cos\theta}\sqrt{\mu_r/\varepsilon_r},$$
$$Z_{R,\mathrm{TM}}(\theta) = Z_R \cos\theta\sqrt{\mu_r/\varepsilon_r}, \qquad \textbf{(1)}$$

where θ is the incident angle, Z_R is the normal impedance of the structure, and μ_r and ε_r denote the relative permeability and permittivity of the material, respectively.

To further deduce the reflection coefficient R, the input impedance Z_{in} of functional motifs is calculated in Eq. (2), which is brought into Eq. (3) to obtain R,
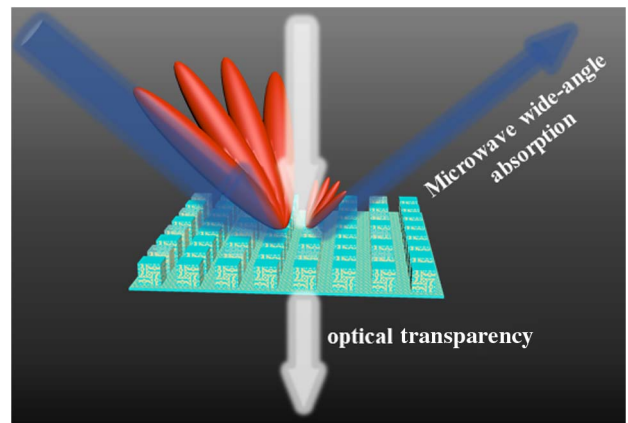

Fig. 1. Schematic diagram of the proposed functional motifs with optical transparency and microwave absorption in wide range and broadband.
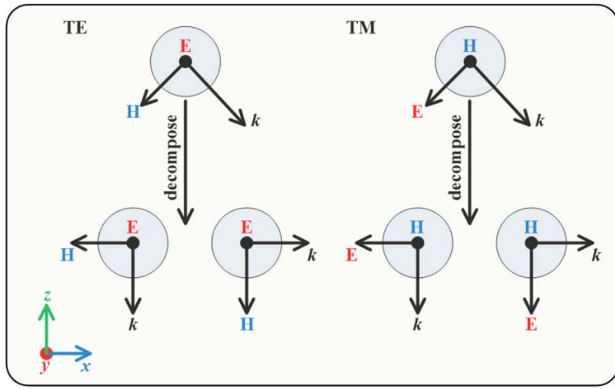
Fig. 2. Vector decomposition of incident waves.

$$Z_{in} = \frac{Z_R(\theta) \cdot Z_d}{Z_R(\theta) + Z_d}, \tag{2}$$

$$R = \frac{\mathrm{Re}\{Z_{in}\} - Z_0}{\mathrm{Re}\{Z_{in}\} + Z_0}. \tag{3}$$

Figure 3 depicts the mechanism of wide-angle absorption. For small incident angles, the bottom layer serves as the main absorbing layer, which contributes to the strong absorption under the vertical component [Fig. 3(a)]. For large incident angles, the top layer serves as the main absorbing layer, which contributes to the strong absorption under the horizontal component [Fig. 3(b)]. In order to decrease and even eliminate the mutual interference between two orthogonal structures, the intelligent optimization algorithm is introduced to the inverse functional motifs design. To prove the proposed paradigm,

the materials with a light transparent characteristic are selected to realize the microwave absorption. As shown in Fig. 4(a), the cubic PMMA substrate ($\varepsilon_r = 2.25 - j0.001$, $\mu_r = 1$), surrounded by ITO films, is stacked on the $N \times N$ bottom structure. Similarly, the bottom structure consists of ITO, PMMA, and ITO layer, where the top ITO layer exhibits the characteristic as resistive film, the middle PMMA layer as dielectric substrate, and the bottom ITO layer as the microwave reflective back plane with 6 Ω/sq. Figures 4(b) and 4(c) show the surface design strategy of the top structure and the bottom structure, respectively. The surface is divided into 20 pixels × 20 pixels, which decide the material in each block. Due to the vector decomposition (Fig. 2) and polarization-independent requirement, symmetry-breaking is utilized to design the same response for TE and TM waves in both vertical and horizontal planes.

In this work, we employ code optimization strategy to design one-eighth of the surface unit, obtaining all the functional motifs by mirror symmetry and central symmetry, where code 0 denotes nothing on the PMMA and code 1 denotes ITO on the PMMA. To get better surface distribution, we set the period gap width of the bottom atom as w_1 and the top atom as w_2, which will be optimized by the intelligent algorithm in the joint simulation (specific information in Appendix A). More importantly, another purpose of gap w_2 is to reduce or even eliminate the impedance interference between two orthogonal structures. To optimize the dimension of cubic side length h, bottom structure period p and thickness d, value of N, gap width w_1 and w_2, surface square resistance values of the bottom meta-atom Ohm_1, and the bottom meta-atom Ohm_2, these parameters are encoded in binary code and are decoded as follows:

$$
\begin{cases}
p = (16 \times p_1 + 8 \times p_2 + 4 \times p_3 + 2 \times p_4 + p_5) \times 0.2 + 4 \\
N = (2 \times n_1 + n_2) + 1 \\
h = [(8 \times h_1 + 4 \times h_2 + 2 \times h_3 + h_4) \times 0.05 + 0.2] \times Np \\
d = (16 \times d_1 + 8 \times d_2 + 4 \times d_3 + 2 \times d_4 + d_5) \times 0.1 + 0.5 \\
w_1 = (4 \times a_1 + 2 \times a_2 + a_3) \times 0.2 \\
w_2 = (4 \times b_1 + 2 \times b_2 + b_3) \times 0.2 + 0.4 \\
\mathrm{Ohm}_1 = (32 \times r_1 + 16 \times r_2 + 8 \times r_3 + 4 \times r_4 + 2 \times r_5 + r_6) \times 5 + 5 \\
\mathrm{Ohm}_2 = (32 \times R_1 + 16 \times R_2 + 8 \times R_3 + 4 \times R_4 + 2 \times R_5 + R_6) \times 5 + 5
\end{cases}
\tag{4}
$$

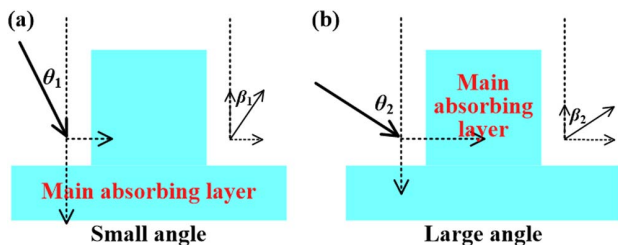where, p_i, n_i, h_i, d_i, a_i, b_i, r_i, and R_i are binary codes—in total, 34.

The absorption rate is calculated as follows:

$$A(w, \theta) = 1 - R^2(w, \theta) - T^2(w, \theta), \tag{5}$$

where w is the frequency and $T(w, \theta)$ is the transmission coefficient of the structure. Here, the microwave reflective plane is designed at the bottom of the whole structure. Thus, $T(w, \theta) = 0$ at the gigahertz regime, and Eq. (5) can be simplified to Eq. (6),

Fig. 3. Absorbing mechanism of the proposed functional motifs. (a) Small incident angle; (b) large incident angle.

$$A(w, \theta) = 1 - R^2(w, \theta). \tag{6}$$

The wide-angle absorber optimization design is a multi-objective optimization problem, so the absorbing efficiency, operating frequency band, and angular stability are considered in the fitness calculation function simultaneously. Here, the optimization goal is to achieve maximum operating bandwidth with an absorption rate more than 90% in the frequency range of 2 to 40 GHz and an incidence angle from 0° to 70° concurrently. The fitness function is set as

$$\text{fitness} = \sum_{i=1}^{4} \text{fitness}(\theta_i),$$

$$\text{fitness}(\theta_i) = 1 - k \cdot \frac{\sum_{j=1}^{n} \Delta F(j, \theta_i)}{f_{\max} - f_{\min}}, \tag{7}$$

where $\Delta F(j, \theta_i)$ is each continuous bandwidth that meets the absorbing requirement under incident angle θ_i (θ_1 to θ_4 are 0°, 40°, 60°, and 70°, respectively), and the $[f_{\min}, f_{\max}] = [2\,\text{GHz}, 40\,\text{GHz}]$. k is the penalty coefficient, which is defined as follows:

$$k = \begin{cases} 1, & 0 \le \text{fitness}_{\max}(\theta_i) - \text{fitness}_{\min}(\theta_i) < 0.2 \\ 0.8, & 0.2 \le \text{fitness}_{\max}(\theta_i) - \text{fitness}_{\min}(\theta_i) < 0.4 , \\ 0.5, & 0.4 \le \text{fitness}_{\max}(\theta_i) - \text{fitness}_{\min}(\theta_i) < 1 \end{cases} \tag{8}$$

where the extreme difference of fitness value under different incident angles will determine the value of k. To attain a balanced wide-angle absorber, the fitness(θ_i) should be maintained close to each other. Meanwhile, Eq. (7) reveals that the wider the valid bandwidth, the smaller the fitness value will be, which means the better absorbing effect should be.

3. RESULTS AND DISCUSSION

After the joint simulation process, the parameters of the proposed structure are optimized as $p = 10$ mm, $h = 24$ mm, $d = 2.7$ mm, $w_1 = 0.2$ mm, $w_2 = 1$ mm, Ohm$_1 = 35\,\Omega/\text{sq}$, Ohm$_2 = 25\,\Omega/\text{sq}$, and $N = 4$. The optimal surface distributions are obtained as shown in Figs. 4(b) and 4(c). Figure 5 depicts the simulated results of the absorption under both TE and TM incident waves. For TE polarization [Fig. 5(a)], the proposed absorber achieves over 10 dB reduction, from
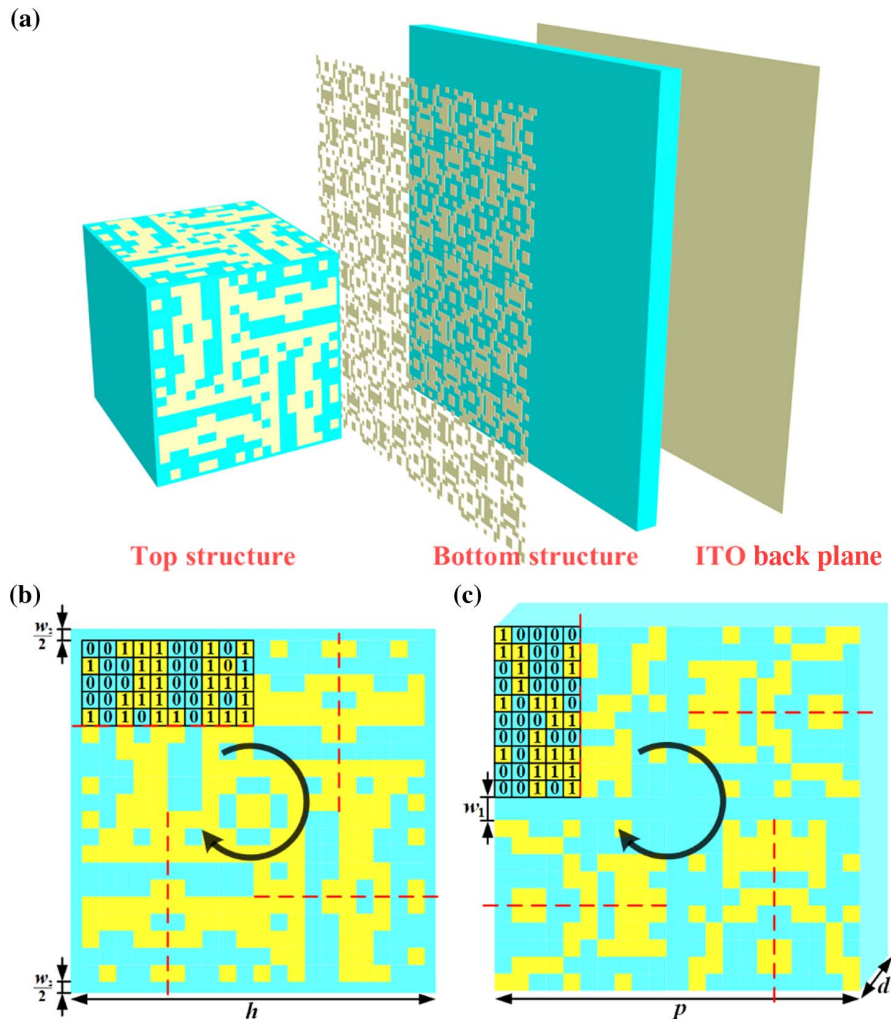

Fig. 4. (a) Functional motifs of the proposed absorber with top, bottom, and back-plane structures, where the square resistance of the ITO back plane is 6 Ω/sq. (b) and (c) are the coding matrix and topology optimization strategy of top and bottom structures, respectively.
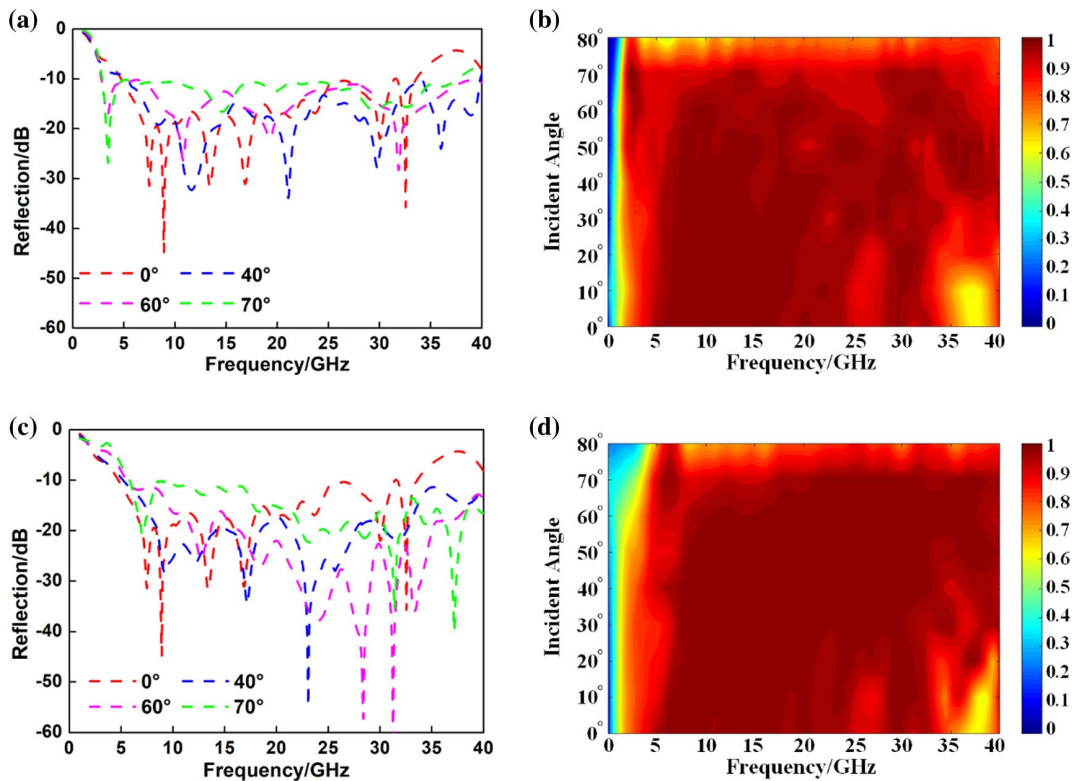
Fig. 5. Simulation curves of absorption. Reflection curves of (a) TE and (c) TM waves at 0°, 40°, 60°, and 70°, respectively; absorption characteristics of (b) TE and (d) TM waves from 0° to 80°, respectively.

4.8 to 34.0 GHz at 0°, 5.0 to 40.0 GHz at 40°, 3.0 to 40 GHz at 60°, and 2.8 to 39.4 GHz at 70°. For TM polarization [Fig. 5(c)], the proposed absorber achieves over 10 dB reduction, from 4.8 to 34.0 GHz at 0°, 5.1 to 40.0 GHz at 40°, 5.2 to 40 GHz at 60°, and 5.2 to 40.0 GHz at 70°. Obviously, the

resonant peaks vary with the polarization and incident angles. Figures 5(b) and 5(d) display the absorption distribution with the frequency and incident angles under TE and TM waves, respectively, where the light red, red, and crimson denote the absorption of over 80%, 90%, and 95%. The
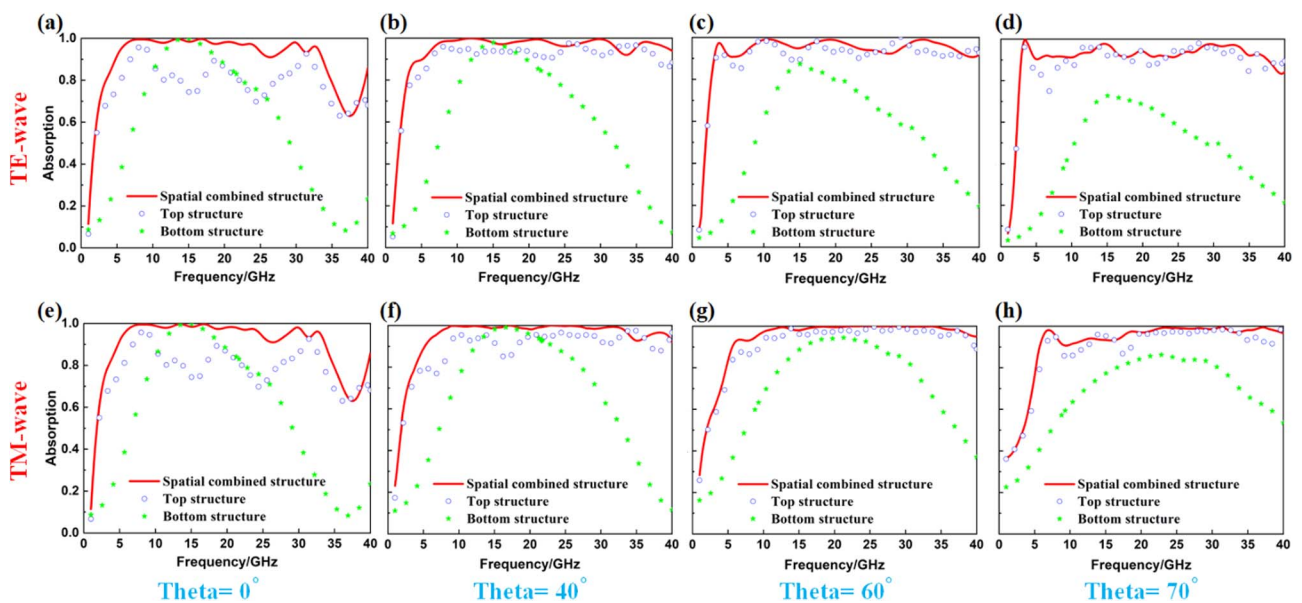

Fig. 6. Absorption curves of spatial combined, top, and bottom structures. (a)–(d) Absorption of TE wave at 0°, 40°, 60°, and 70°, respectively; (e)–(h) absorption of TM wave at 0°, 40°, 60°, and 70°, respectively.
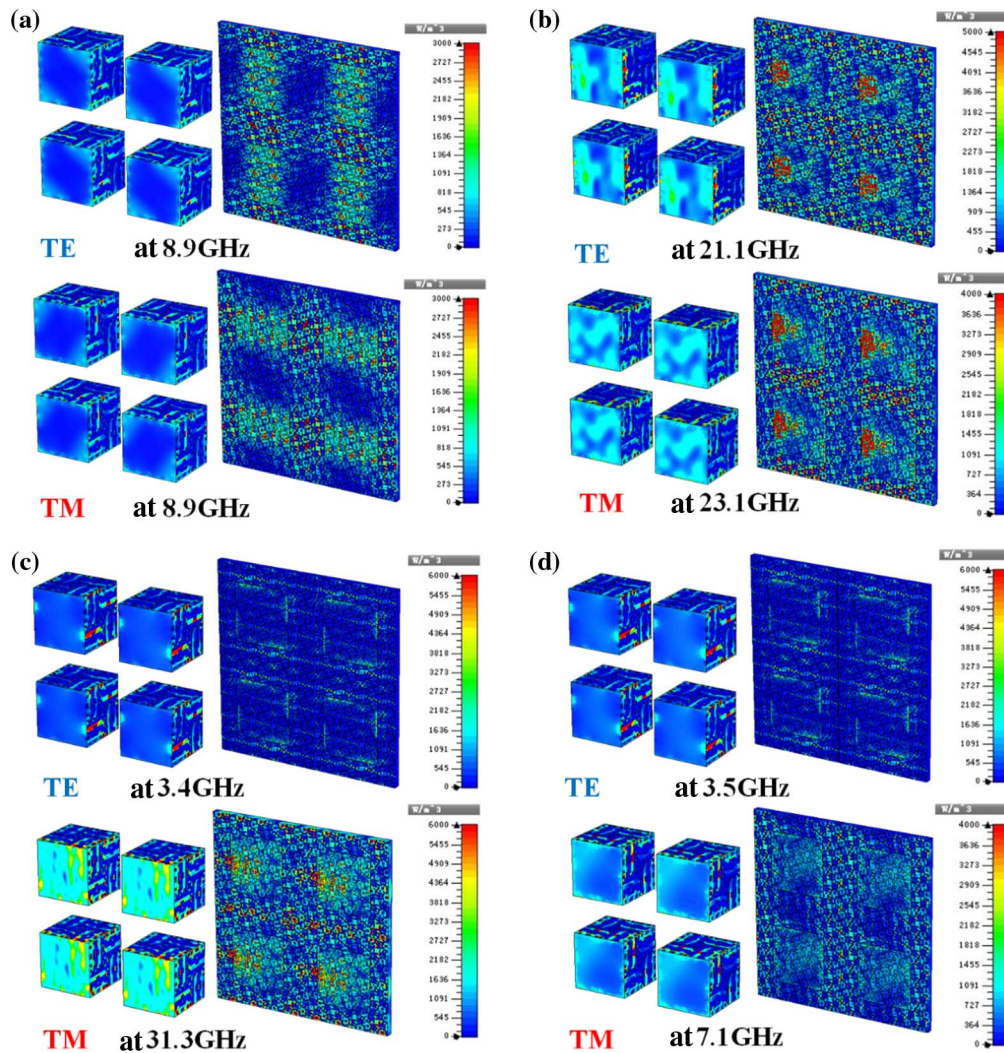
Fig. 7. Loss distribution of different incident angles and polarization at their own maximum resonance peaks. (a) For 0°, both TE and TM at 8.9 GHz; (b) for 40°, TE at 21.1 GHz and TM at 23.1 GHz; (c) for 60°, TE at 3.4 GHz and TM at 31.3 GHz; (d) for 70°, TE at 3.5 GHz and TM at 7.1 GHz.

absorption performance is so stable that this inverse polarization-independent design method achieves more than 148.7% fractional bandwidth (FBW) and exhibits forceful angular absorption stability from 0° to 70° for both TE and TM waves.

Especially for TE polarization, this absorber, realizing a better performance than TM polarization at wide angles, achieves more than 172.1% FBW from 60° to 70°, which is a breakthrough in the design of wide-angle dual polarization absorption.
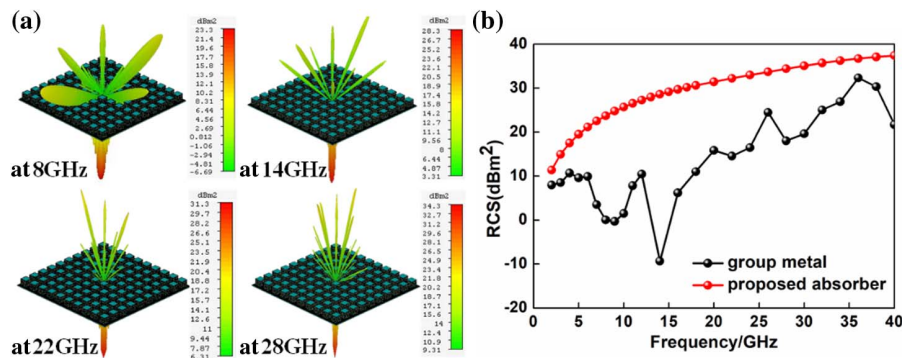

Fig. 8. (a) Simulated 3D far-field patterns under normal incidence at 8, 14, 22, and 28 GHz; (b) simulated monostatic RCS of the designed absorber and group metal from 2 to 40 GHz.
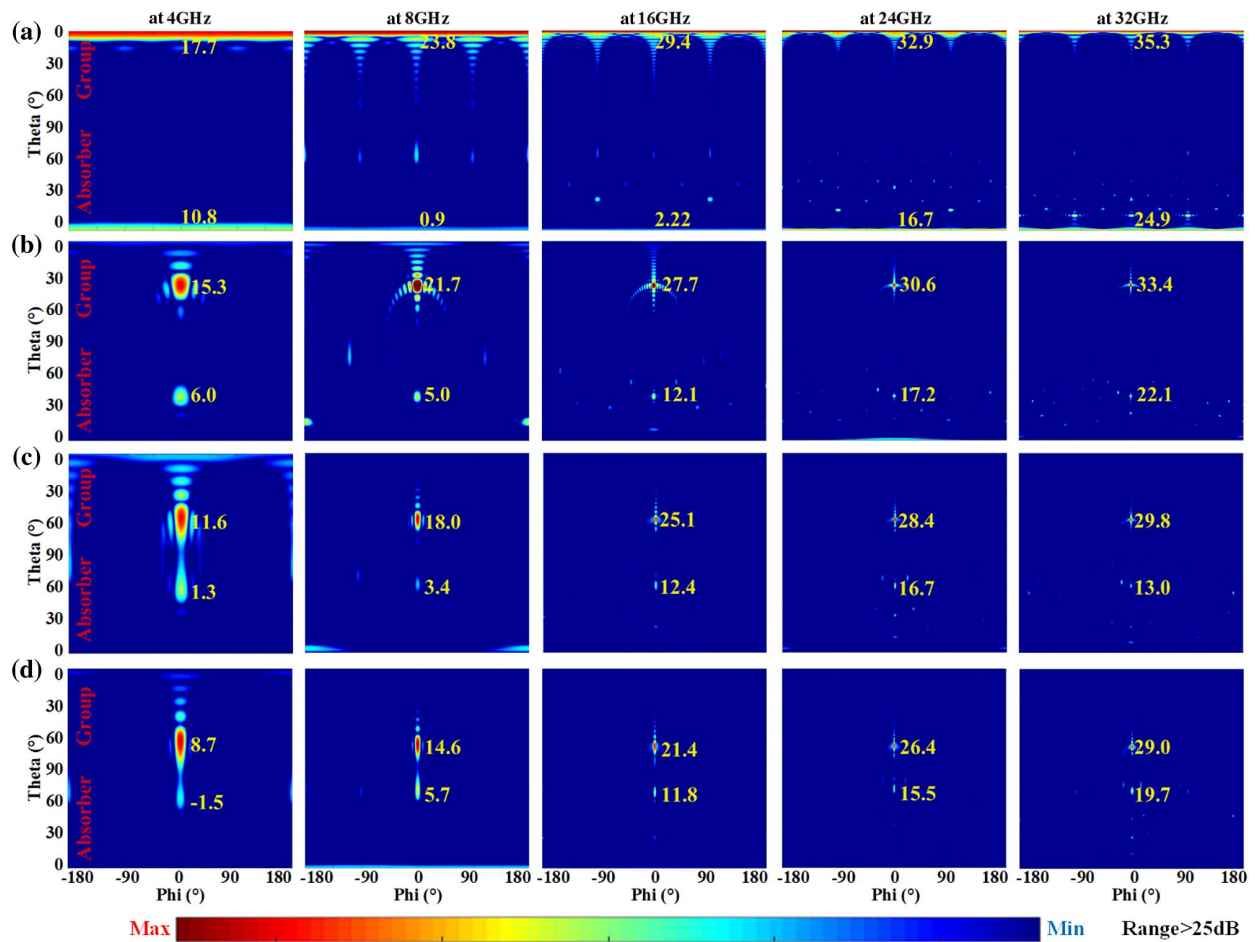
Fig. 9.   2D far-field patterns of both absorber and group metal from 4 to 32 GHz in range of 0° to 70° incidences. (a) 0°, (b) 40°, (c) 60°, and (d) 70°. The yellow values mark the value of maximum RCS points, and the range of minimum to maximum is over 25 dB.

In order to validate the improvement from the multidimensional design of functional motifs, the absorption of functional motifs, only the top structure and only the bottom structure are discussed in Fig. 6. For both TE and TM polarization waves, the absorptions of top and bottom structures are simulated from 0° to 70°, respectively, and compared with the spatial structure. Figures 6(a)–6(d) showcase each absorption curve of these three structures under TE waves from 0° to 70°. Under small incident angles [Figs. 6(a) and 6(b)], the top structure cannot exhibit strong absorption, while the bottom structure can assist the top structure to improve performance. Under large incident angles [Figs. 6(c) and 6(d)], the top structure has performance very close to the spatial structure, while the absorption of the bottom structure obviously decreases. Figures 6(e)–6(h) showcase each absorption curve of these three structures under TM waves from 0° to 70°. Similar to the results for the TE wave, the top structure shows the strong absorption in the range of large angles, and the bottom structure can assist the top structure to increase the absorption in the range of small angles. Importantly, the absorbing phenomenon of spatial structure has verified our design theme, that the bottom and top structures are utilized to mostly respond to vertical and horizontal waves, respectively (shown in Fig. 3).

To further understand the mechanism of the designed absorber in the range of wide angles, we have monitored the power loss density of the proposed metastructure. Figure 7 shows the energy loss distribution of the strongest resonant peaks under TE and TM waves from 0° to 70°. For incident angle 0°, Fig. 7(a) illustrates the loss distribution of both the top and bottom structures at 8.9 GHz for both TE and TM waves, where most of the energy loss distributes in the horizontal area. For incident angle 40°, Fig. 7(b) depicts the loss distribution at 21.1 GHz for the TE wave and 23.1 GHz for the TM wave, where the energy loss in the horizontal area accounts for a little more than the vertical area around the top structure. Figures 7(a) and 7(b) reveal the fact that the small incident angles have mainly been solved by the bottom structure, which is coherent with our design principle for absorption under small incident angles. For incident angle 60°, Fig. 7(c) showcases the power loss density at 3.4 GHz for the TE wave and 31.3 GHz for the TM waves. With the increase of incident angle, the energy loss in the vertical area around the top structure starts to account for more than in the horizontal area, especially for the TE wave. Meanwhile, the absorption of TE expands to low frequency. For incident angle 70°, Fig. 7(d) displays the loss distribution at 3.5 GHz for the TE wave and 7.1 GHz for the TM wave. In

contrast to small incident angles, most of the energy loss distributes in the vertical area, which verifies our proposed design method to absorb EM waves in large incident angles. Moreover, the frequency of resonant peaks varies with incident polarization and angles, revealing the operating mechanism that the broadband polarization-independent absorption is implemented by the coupling of electric and magnetic resonances.

In addition, the far-field patterns of the designed absorber with 10 × 10 units and group metal of the same size are simulated. Figure 8(a) illustrates the simulated 3D far-field patterns of both absorber and metal under normal incidence at 8, 14, 22, and 28 GHz. Compared to the total reflection at the

bottom side (control group metal), the proposed absorber achieves the wavefront absorption at the top side. To directly show the benefit brought by the designed absorber, Fig. 8(b) gives the monostatic radar cross section (RCS) of the designed absorber and control group metal. The over 10 dB reduction is achieved from 5 to 34 GHz, which is highly coherent with the absorbing operating band under normal incidence. For visually analyzing the EM field distribution, the 3D far-field information is transformed to the 2D patterns shown in Fig. 9, where the plane diagrams consist of the far-field value at each elevation angle θ and azimuth angle φ. To depict the absorbing effect clearly, the RCS of both the designed absorber and the
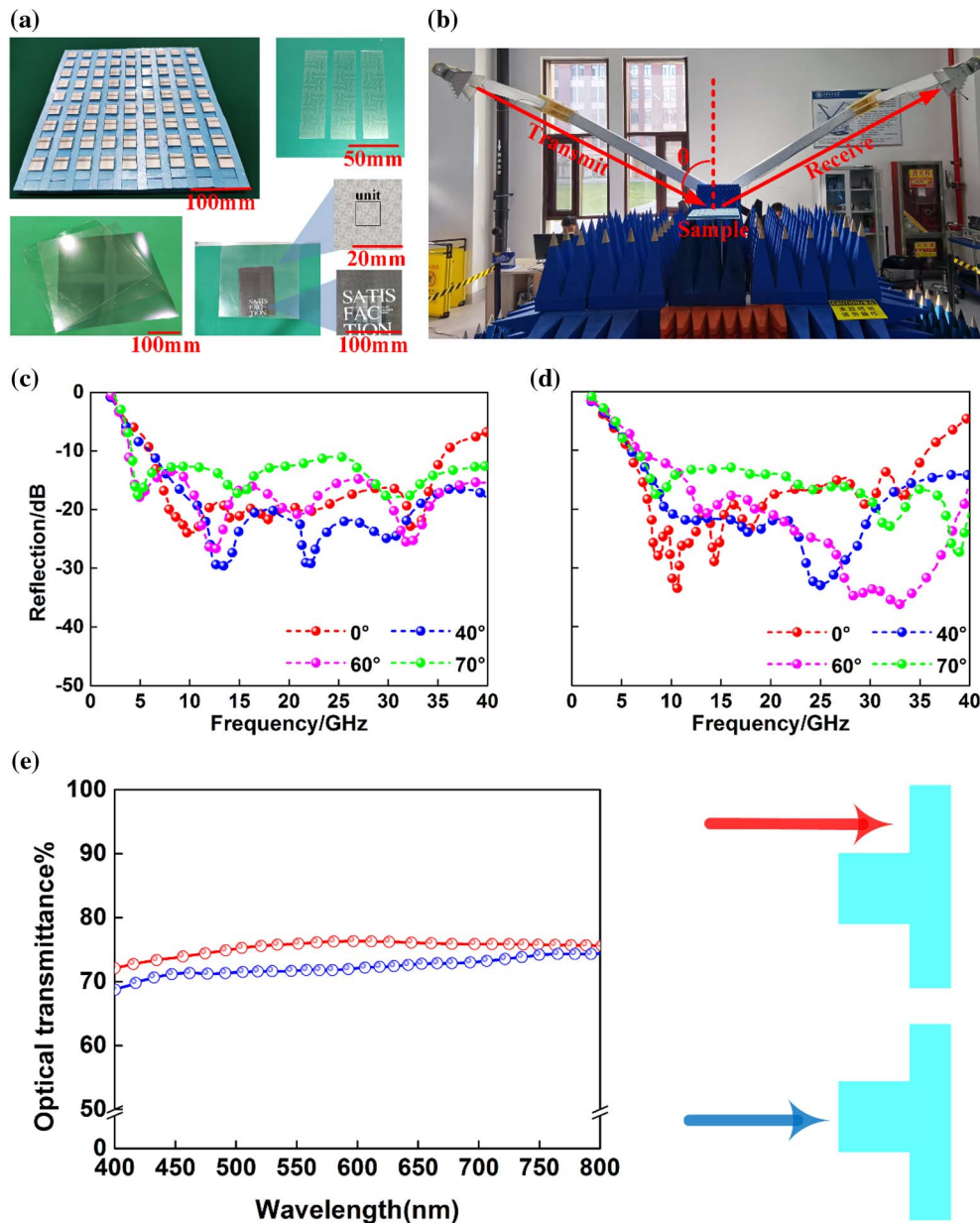

Fig. 10. (a) Photograph of the fabricated prototype with the inset showing the functional motifs; (b) experimental setup of mirror reflection measurement; (c) and (d) measured reflection curves of TE and TM waves under 0°, 40°, 60°, and 70° incidences, respectively; (e) measured optical transmittance of the prototype, where red and blue lines represent the transmittance of the red and blue arrow incident types, respectively.

control group at the direction $\theta = \theta_i$ and $\varphi = 0°$ is marked at 4, 8, 16, 24, and 32 GHz, respectively. Apparently, the marked points are also the maximum value in the spatial areas. Thus, the RCS reduction effect of the absorber can be derived from the marked point comparison between absorber and the control group. For 0° and 40° incidences [Figs. 9(a) and 9(b)], the designed absorber expresses over 10 dB reduction at 8, 16, 24, and 32 GHz within the operating band, while at outband 4 GHz, the reduction is only 6.9 dB at 0° and 8.7 dB at 40°. For 60° and 70° incidences [Figs. 9(c) and 9(d)], owing to the wide operating band under large angles, the designed absorber achieves over 10 dB reduction at 4, 8, 16, 24, and 32 GHz. Above all, the wide-angle broadband absorption has been strongly proved from different aspects such as reflection, power loss density, and far-field distribution, which all verify the good performance of our proposed absorber.

To prove the proposed design paradigm and the simulated performance experimentally, a prototype [Fig. 10(a)] with size 400 mm × 400 mm × 26.7 mm is fabricated. The 6 Ω/sq, 25 Ω/sq, and 35 Ω/sq ITO films are taken by magnetron sputtering with different tin–oxygen contents. To get the designed PMMA structures, precise matching is utilized to slice and polish each PMMA prototype. For microwave testing, the top

structure is placed in a foam mold ($\varepsilon_r \approx 1.01$) and is then stacked on the bottom structure. In the foam mold, the ITO films of cubes are attached to the four faces of the cubes by electrostatic attachment. The whole prototype is placed in the mirror reflection test platform [Fig. 10(b)], which is surrounded by the microwave absorbing wedges. In the measurement process, two pairs of broadband antennas (2–18 GHz and 18–40 GHz, respectively) serve as a transmitter and receiver. Figures 10(c) and 10(d) showcase the measured reflection curves of TE and TM waves, respectively. The experimental results coincide with the simulated results practically from 0° to 70°, verifying the design theory for wide-angle absorption. For the optical frequency, the transmittance of the prototype is tested as being one of two types [Fig. 10(e)]. The red curve shows that the optical wave illuminates as the schematic of the red arrow type, which only penetrates the bottom structure; the optical transmittance is over 71.6%, from 400 to 800 nm. The blue curve denotes that the optical wave illuminates as the schematic of the blue arrow type, which penetrates both the top and bottom structures; the optical transmittance is over 69.5%, from 400 to 800 nm. In this work, the duty ratio of the top structure is calculated as $(h/Np)^2 = 0.36$, and the average optical transmittance is derived at over 70.8%, from 400 to 800 nm, which ensures high transparent performance for the naked eye.
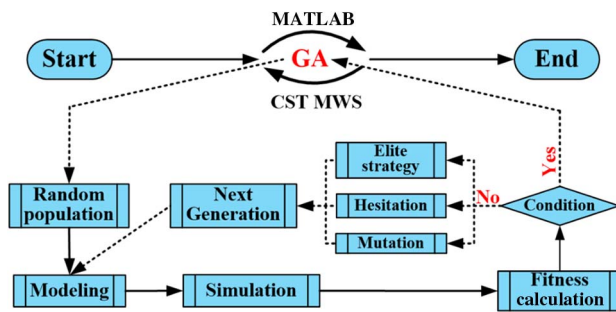
4. CONCLUSION

In summary, a general strategy was proposed for ultrabroadband and wide-angle absorbers via multidimensional design of functional motifs. By coupling the orthogonal meta-atoms, functional motifs exhibit the angular tolerance of impedance matching. To broaden the operating frequency band and maintain angular tolerance simultaneously, an intelligent algorithm is utilized to search the optimal structure parameters. As a demonstration, a wide-angle broadband polarization-independent absorber is designed and verified in microwave regimes. What is more, the proposed functional motifs can be attached with optical transparency function at will, which
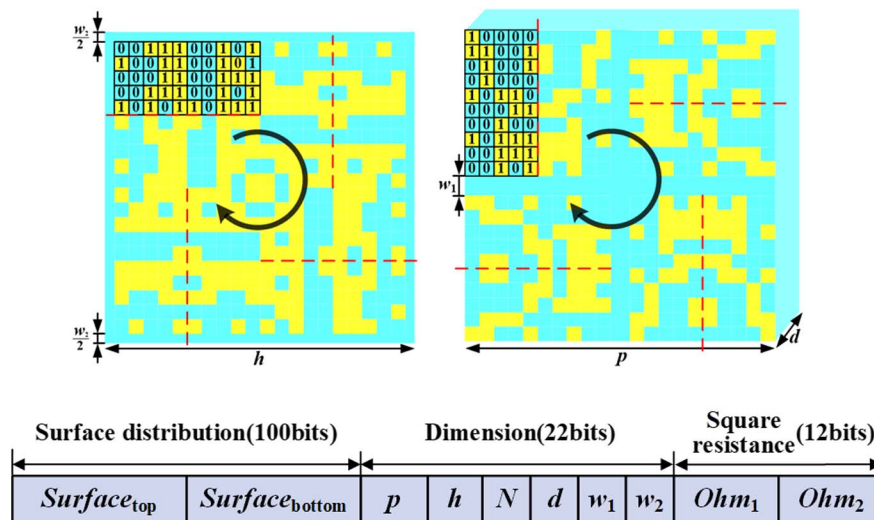

Fig. 11. Flow chart of the joint simulation.

Fig. 12. Coding expression of the structure parameters.

strongly proves the feasibility of the multidimensional design. We firmly believe that the proposed method can be expanded from microwave to infrared and optical regimes, and the proposed design mentality can be extended to be multispectrum-compatible as an optical hologram and infrared (microwave) stealth-compatible, infrared and microwave
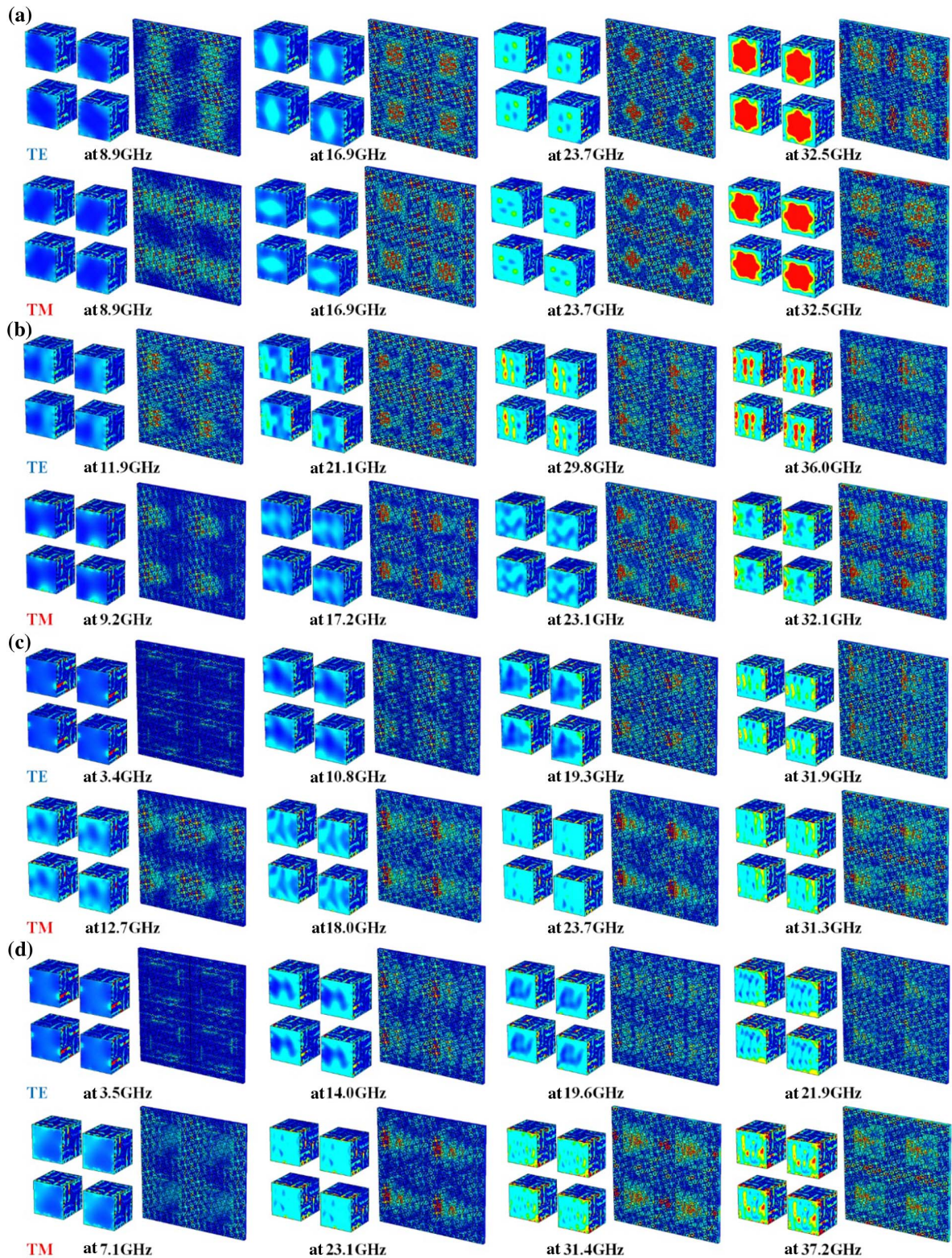

Fig. 13. Power loss density of the proposed functional motifs under different incident angles and polarization at each resonant peak. (a) 0°, (b) 40°, (c) 60°, and (d) 70°.

stealth-compatible, optical visibility and wavefront manipulation-compatible, etc.

APPENDIX A: OPTIMIZATION STRATEGY OF BROADBAND WIDE-ANGLE IMPEDANCE MATCHING FOR STRONG ABSORPTION IN FULL-POLARIZATION STATES

The main method of optimization is to obtain the optimal parameters of each dimension and surface distribution, respectively, by genetic algorithm (GA), particle swarm optimization (PSO), and so on. In this work, we adopted GA to improve the performance of wide-angle absorption in both TE and TM polarizations. As shown in Fig. 4, the parameters of the period structure are set by the optimization scope as in Eq. (4). Here, we mainly introduce the use of joint simulation in the optimization process. A joint simulation is performed for the propagating metasurface with the commercial software CST and optimized by GA in MATLAB, as shown in Fig. 11. The joint simulation starts from the MATLAB program, which generates a random population with size 200. Each individual of the population consists of a 137-gene chromosome to determine the structural parameters.

Figure 12 shows the gene sequence, which defines the surface distribution, structural dimension, and square resistance of ITO films. Each individual is modeled and simulated in the software CST Microwave Studio (MWS), and the result is then analyzed and iterated by the optimization algorithm in MATLAB automatically. For the GA program, we set the iteration times as 40, cross rate as 0.8, mutation rate as 0.1, and elitist preservation rate as 0.05. For the EM simulation part in CST, the boundary conditions of the x and y directions are set as a unit cell, and the z direction is set as open added space. To calculate frequency-amplitude curves, the frequency domain solver is selected with two ports: TE and TM polarizations. In this work, the paradigm of the proposed spatial combined structure with optimization strategy aims to complete the polarization-independent broadband wide-angle absorption.

APPENDIX B: MULTIRESONANT ENERGY LOSS DISTRIBUTION IN THE ULTRABROADBAND

To further understand the mechanism of the broadband polarization-independent performance in the range of wide angles, we have monitored the power loss density of the proposed metastructure shown in Fig. 13. For incident angle 0°, Fig. 13(a) illustrates the loss distribution of both the top and bottom structures at four resonant peaks (8.9, 16.9, 23.7, and 32.5 GHz) for both TE and TM waves, where most of the energy loss distributes in the horizontal area, except that the cubic substrate expresses the high loss density at higher frequencies, which is due to the thick scale of the dielectric. For incident angle 40°, Fig. 13(b) depicts the loss distribution at the four resonant peaks (11.9, 21.1, 29.8, and 36.1 GHz for TE, and 9.2, 17.2, 23.1, and 32.1 GHz for TM), respectively. For incident angle 60°, Fig. 13(c) showcases the power loss density at the four resonant peaks (3.4, 10.8, 19.3, and 31.9 GHz for TE, and 12.7, 18.0, 23.7, and 31.3 GHz for TM), respectively. For incident angle 70°, Fig. 13(d) displays the loss dis-

tribution at the resonant peaks (3.46, 14.1, 19.6, and 29.1 GHz for TE, and 7.1, 23.1, 31.4, and 37.2 GHz for TM). In contrast to 0°, most of the energy loss distributes in the vertical area, except that there is some energy loss in the horizontal area at high frequencies, which is due to the inherent absorption performance of the bottom structure at high frequencies.

Disclosures. The authors declare that they have no known competing financial interests or personal relationships that could have appeared to influence the work reported in this paper.

Data Availability. Data underlying the results presented in this paper may be obtained from the authors upon reasonable request.

†These authors contributed equally to this paper.

REFERENCES

1. M. M. Ardehali, M. Shahrestani, and C. C. Adams, "Energy simulation of solar assisted absorption system and examination of clearness index effects on auxiliary heating," Energy Convers. Manage. **48**, 864–870 (2007).
2. Q. He, S. Wang, S. Zeng, and Z. Zheng, "Experimental investigation on photothermal properties of nanofluids for direct absorption solar thermal energy systems," Energy Convers. Manage. **73**, 150–157 (2013).
3. Y. Yang, Q. Jin, D. Mao, J. Qi, Y. Wei, R. Yu, A. Li, S. Li, H. Zhao, Y. Ma, L. Wang, W. Hu, and D. Wang, "Dually ordered porous TiO₂-rGO composites with controllable light absorption properties for efficient solar energy conversion," Adv. Mater. **29**, 1604795 (2017).
4. D. Chung, "Electromagnetic interference shielding effectiveness of carbon materials," Carbon **39**, 279–285 (2001).
5. X. Lu, W. Zhang, C. Wang, T. Wen, and Y. Wei, "One-dimensional conducting polymer nanocomposites: synthesis, properties and applications," Prog. Polym. Sci. **36**, 671–712 (2011).
6. E. F. Knott, J. F. Schaeffer, and M. T. Tulley, *Radar Cross Section* (SciTech, 2004).
7. H. Mei, D. Yang, L. Yao, W. Yang, X. Zhao, Y. Yao, L. Cheng, L. Zhang, and K. G. Dassios, "Broadening the absorption bandwidth by novel series–parallel cross convex–concave structures," J. Mater. Chem. C **9**, 5411–5424 (2021).
8. B. Quan, X. Liang, G. Xu, Y. Cheng, Y. Zhang, W. Liu, G. Ji, and Y. Du, "A permittivity regulating strategy to achieve high-performance electromagnetic wave absorbers with compatibility of impedance matching and energy conservation," New J. Chem. **41**, 1259–1266 (2017).
9. C. Song, Y. Huang, P. Carter, J. Zhou, S. Yuan, Q. Xu, and M. Kod, "A novel six-band dual CP rectenna using improved impedance matching technique for ambient RF energy harvesting," IEEE Trans. Antennas Propag. **64**, 3160–3171 (2016).
10. X. Li, C. Wen, L. Yang, R. Zhang, X. Li, Y. Li, and R. Che, "MXene/FeCo films with distinct and tunable electromagnetic wave absorption by morphology control and magnetic anisotropy," Carbon **175**, 509–518 (2021).
11. P. Liu, S. Gao, G. Zhang, Y. Huang, W. You, and R. Che, "Hollow engineering to Co@N-doped carbon nanocages via synergistic

protecting-etching strategy for ultrahigh microwave absorption," Adv. Funct. Mater. **31**, 2102812 (2021).

12. W. Gu, J. Tan, J. Chen, Z. Zhang, Y. Zhao, J. Yu, and G. Ji, "Multifunctional bulk hybrid foam for infrared stealth, thermal insulation, and microwave absorption," ACS Appl. Mater. Interfaces **12**, 28727–28737 (2020).

13. X. Cui, X. Liang, W. Liu, W. Gua, G. Ji, and Y. Du, "Stable microwave absorber derived from 1D customized heterogeneous structures of Fe₃N@C," Chem. Eng. J. **381**, 122589 (2020).

14. Y. Sun, J. Zhang, Y. Zong, X. Deng, H. Zhao, J. Feng, M. He, X. Li, Y. Peng, and X. Zheng, "Crystalline–amorphous permalloy@iron oxide core–shell nanoparticles decorated on graphene as high-efficiency, lightweight, and hydrophobic microwave absorbents," ACS Appl. Mater. Interfaces **11**, 6374–6383 (2019).

15. E. Nahvi, I. Liberal, and N. Engheta, "Nonlinear metamaterial absorbers enabled by photonic doping of epsilon-near-zero metastructures," Phys. Rev. B **102**, 035404 (2020).

16. W. Tian, J. Li, Y. Liu, R. Ali, Y. Guo, L. Deng, N. Mahmood, and X. Jian, "Atomic-scale layer-by-layer deposition of FeSiAl@ZnO@Al₂O₃ hybrid with threshold anti-corrosion and ultra-high microwave absorption properties in low-frequency bands," Nano-Micro Lett. **13**, 161 (2021).

17. Y. Cui, H. Yao, J. Zhang, T. Zhang, Y. Wang, L. Hong, K. Xian, B. Xu, S. Zhang, J. Peng, Z. Wei, F. Gao, and J. Hou, "Over 16% efficiency organic photovoltaic cells enabled by a chlorinated acceptor with increased open-circuit voltages," Nat. Commun. **10**, 2515 (2019).

18. S. Guddala and S. A. Ramakrishna, "Optical limiting by nonlinear tuning of resonance in metamaterial absorbers," Opt. Lett. **41**, 5150–5153 (2016).

19. S. Saggar, K. D. Deshmukh, S. K. M. McGregor, M. Hasan, A. Shukla, J. S. Agawane, N. Nayak, E. Gann, L. Thomsen, A. Kumar, C. R. McNeill, S. Lo, and E. B. Namdas, "Impact of polymer molecular weight on polymeric photodiodes," Adv. Opt. Mater. **10**, 2101890 (2021).

20. Y. Qiao, Z. Yao, X. Wang, X. Zhang, C. Bai, Q. Li, K. Chen, Z. Li, and T. Zheng, "Lattice composites with embedded short carbon fiber/Fe₃O₄/epoxy hollow spheres for structural performance and microwave absorption," Mater. Des. **188**, 108427 (2020).

21. S. Guddala, R. Kumar, and S. A. Ramakrishna, "Thermally induced nonlinear optical absorption in metamaterial perfect absorbers," Appl. Phys. Lett. **106**, 111901 (2015).

22. H. Mei, W. Yang, X. Zhao, L. Yao, Y. Yao, C. Chen, and L. Cheng, "In-situ growth of SiC nanowires@ carbon nanotubes on 3D printed metamaterial structures to enhance electromagnetic wave absorption," Mater. Des. **197**, 109271 (2021).

23. J. B. Pendry, "Negative refraction makes a perfect lens," Phys. Rev. Lett. **85**, 3966–3969 (2000).

24. D. R. Smith, J. B. Pendry, and M. C. Wiltshire, "Metamaterials and negative refractive index," Science **305**, 788–792 (2004).

25. J. B. Pendry, D. Schurig, and D. R. Smith, "Controlling electromagnetic fields," Science **312**, 1780–1782 (2006).

26. N. Yu, P. Genevet, M. A. Kats, F. Aieta, J. P. Tetienne, F. Capasso, and Z. Gaburro, "Light propagation with phase discontinuities: generalized laws of reflection and refraction," Science **334**, 333–337 (2011).

27. X. Ding, F. Monticone, K. Zhang, L. Zhang, D. Gao, S. N. Burokur, A. de Lustrac, Q. Wu, C. Qiu, and A. Alù, "Ultrathin Pancharatnam-Berry metasurface with maximal cross-polarization efficiency," Adv. Mater. **27**, 1195–1200 (2015).

28. S. Sun, K. Yang, C. Wang, T. Juan, W. T. Chen, C. Y. Liao, Q. He, S. Xiao, W. Kung, G. Guo, L. Zhou, and D. P. Tsai, "High-efficiency broadband anomalous reflection by gradient meta-surfaces," Nano Lett. **12**, 6223–6229 (2012).

29. A. Epstein and G. V. Eleftheriades, "Synthesis of passive lossless metasurfaces using auxiliary fields for reflectionless beam splitting and perfect reflection," Phys. Rev. Lett. **117**, 256103 (2016).

30. Y. Sun, X. Zhang, Q. Yu, W. Jiang, and T. J. Cui, "Infrared-controlled programmable metasurface," Sci. Bull. **65**, 883–888 (2020).

31. W. Guo, G. Wang, X. Luo, H. Hou, K. Chen, and Y. Feng, "Ultrawideband spin-decoupled coding metasurface for independent dual-channel wavefront tailoring," Ann. Phys. **532**, 1900472 (2020).

32. L. Gao, Q. Cheng, J. Yang, S. Ma, J. Zhao, S. Liu, H. Chen, Q. He, W. Jiang, H. Ma, Q. Wen, L. Liang, B. Jin, W. Liu, L. Zhou, J. Yao, P. Wu, and T. Cui, "Broadband diffusion of terahertz waves by multi-bit coding metasurfaces," Light Sci. Appl. **4**, e324 (2015).

33. Y. Pang, Y. Li, B. Qu, M. Yan, J. Wang, S. Qu, and Z. Xu, "Wideband RCS reduction metasurface with a transmission window," IEEE Trans. Antennas Propag. **68**, 7079–7087 (2020).

34. C. Zhang, C. Long, S. Yin, R. Song, B. Zhang, J. Zhang, D. He, and Q. Cheng, "Graphene-based anisotropic polarization meta-filter," Mater. Des. **206**, 109768 (2021).

35. A. Murugesan, D. Natarajan, and K. T. Selvan, "Low-cost, wideband checkerboard metasurfaces for monostatic RCS reduction," IEEE Antennas Wireless Propag. Lett. **20**, 493–497 (2021).

36. Y. Xi, W. Jiang, T. Hong, K. Wei, and S. Gong, "Wideband and wide-angle radar cross section reduction using a hybrid mechanism metasurface," Opt. Express **29**, 22427–22441 (2021).

37. Q. Zheng, C. Guo, J. Ding, and G. A. E. Vandenbosch, "A broadband low-RCS metasurface for CP patch antennas," IEEE Trans. Antennas Propag. **69**, 3529–3534 (2020).

38. Q. Yuan, H. Ma, J. Jiang, J. Wang, Y. Li, S. Zhao, and S. Qu, "Al₂O₃ based ceramic with polarization controlled meta-structure for high-temperature broadband backward scattering manipulation," J. Alloys Compd. **854**, 157168 (2021).

39. G. Zheng, H. Mühlenbernd, M. Kenney, G. Li, T. Zentgraf, and S. Zhang, "Metasurface holograms reaching 80% efficiency," Nat. Nanotechnol. **10**, 308–312 (2015).

40. L. Huang, S. Zhang, and T. Zentgraf, "Metasurface holography: from fundamentals to applications," Nanophotonics **7**, 1169–1190 (2018).

41. Y. Cheng, Y. Li, H. Wang, H. Chen, W. Wan, J. Wang, L. Zheng, J. Zhang, and S. Qu, "Ohmic dissipation-assisted complex amplitude hologram with high quality," Adv. Opt. Mater. **9**, 2002242 (2021).

42. H. Wang, Z. Qin, L. Huang, Y. Li, R. Zhao, H. Zhou, H. He, J. Zhang, and S. Qu, "Metasurface with dynamic chiral meta-atoms for spin multiplexing hologram and low observable reflection," PhotoniX **3**, 1 (2022).

43. Z. Li, C. Chen, Z. Guan, J. Tao, S. Chang, Q. Dai, Y. Xiao, Y. Cui, Y. Wang, S. Yu, G. Zheng, and S. Zhang, "Three-channel metasurfaces for simultaneous meta-holography and meta-nanoprinting: a single-cell design approach," Laser Photon. Rev. **14**, 2000032 (2020).

44. L. Li, H. Ruan, C. Liu, Y. Li, Y. Shuang, A. Alù, C. Qiu, and T. Cui, "Machine-learning reprogrammable metasurface imager," Nat. Commun. **10**, 1082 (2019).

45. N. I. Landy, S. Sajuyigbe, J. J. Mock, D. R. Smith, and W. J. Padilla, "Perfect metamaterial absorber," Phys. Rev. Lett. **100**, 207402 (2008).

46. Y. J. Yoo, Y. J. Kim, P. V. Tuong, J. Y. Rhee, K. W. Kim, W. H. Jang, Y. H. Kim, H. Cheong, and Y. Lee, "Polarization-independent dual-band perfect absorber utilizing multiple magnetic resonances," Opt. Express **21**, 32484–32490 (2013).

47. L. Li, Y. Yang, and C. Liang, "A wide-angle polarization-insensitive ultra-thin metamaterial absorber with three resonant modes," J. Appl. Phys. **110**, 063702 (2011).

48. X. Luo, Z. Cheng, X. Zhai, Z. Liu, S. Li, J. Liu, L. Wang, Q. Lin, and Y. Zhou, "A tunable dual-band and polarization-insensitive coherent perfect absorber based on double-layers graphene hybrid waveguide," Nanoscale Res. Lett. **14**, 337 (2019).

49. Z. Zhou, K. Chen, J. Zhao, P. Chen, T. Jiang, B. Zhu, Y. Feng, and Y. Li, "Metasurface Salisbury screen: achieving ultra-wideband microwave absorption," Opt. Express **25**, 30241–30252 (2017).

50. K. Zhang, X. Cheng, Y. Zhang, M. Chen, H. Chen, Y. Yang, W. Song, and D. Fang, "Weather-manipulated smart broadband electromagnetic metamaterials," ACS Appl. Mater. Interfaces **10**, 40815–40823 (2018).

51. D. H. Le and S. Lim, "Four-mode programmable metamaterial using ternary foldable origami," ACS Appl. Mater. Interfaces **11**, 28554–28561 (2019).

52. Q. Chen, M. Guo, D. Sang, Z. Sun, and Y. Fu, "RCS reduction of patch array antenna using anisotropic resistive metasurface," IEEE Antennas Wireless Propag. Lett. **18**, 1223–1227 (2019).

53. Q. Chen, D. Sang, M. Guo, and Y. Fu, "Miniaturized frequency-selective rasorber with a wide transmission band using circular spiral resonator," IEEE Trans. Antennas Propag. **67**, 1045–1052 (2018).

54. Y. Shen, J. Zhang, Y. Meng, Z. Wang, Y. Pang, J. Wang, H. Ma, and S. Qu, "Merging absorption bands of plasmonic structures via dispersion engineering," Appl. Phys. Lett. **112**, 254103 (2018).

55. L. Zhou and Z. Shen, "Absorptive coding metasurface with ultrawide-band backscattering reduction," IEEE Antennas Wireless Propag. Lett. **19**, 1201–1205 (2020).

56. C. Li, Z. Xu, L. Lin, S. Guo, Y. He, L. Miao, and J. Jiang, "Ultralow scattering and broadband metasurface using phase adjustable FSS elements embedded with lumped resistors," IEEE Antennas Wireless Propag. Lett. **20**, 793–797 (2021).

57. T. Shao, H. Ma, J. Wang, M. Yan, M. Feng, Z. Yang, Q. Zhou, J. Wang, Y. Meng, S. Zhao, and S. Qu, "Ultra-thin and high temperature NiCrAlY alloy metamaterial enhanced radar absorbing coating," J. Alloys Compd. **832**, 154945 (2020).

58. X. Jiang, S. Deng, M. Whangbo, and G. Guo, "Material research from the viewpoint of functional motifs," Natl. Sci. Rev. **9**, nwac017 (2022).

59. M. E. King, M. V. F. Guzmana, and M. B. Ross, "Material strategies for function enhancement in plasmonic architectures," Nanoscale **14**, 602–611 (2022).

60. S. Jiang, J. Li, J. Li, G. Zhang, H. Liu, and F. Yi, "Genetic optimization of plasmonic metamaterial absorber towards dual-band infrared imaging polarimetry," Opt. Express **28**, 22617–22629 (2020).

61. J. Chen, W. Ding, X.-M. Li, X. Xi, K. Ye, H. Wu, and R. Wu, "Absorption and diffusion enabled ultrathin broadband metamaterial absorber designed by deep neural network and PSO," IEEE Antennas Wireless Propag. Lett. **20**, 1993–1997 (2021).

62. W. Zhang, H. Qi, Z. Yu, M. He, Y. Ren, and Y. Li, "Optimization configuration of selective solar absorber using multi-island genetic algorithm," Sol. Energy **224**, 947–955 (2021).

63. H. Zhang, Y. Wang, K. Lu, H. Zhao, D. Yu, and J. Wen, "SAP-Net: deep learning to predict sound absorption performance of metaporous materials," Mater. Des. **212**, 110156 (2021).

64. H. On, L. Jeong, M. Jung, D. Kang, J. Park, and H. Lee, "Optimal design of microwave absorber using novel variational autoencoder from a latent space search strategy," Mater. Des. **212**, 110266 (2021).

65. Q. Yuan, H. Ma, S. Sui, J. Wang, Y. Meng, Y. Pang, and S. Qu, "A transgenic genetic algorithm design method that helps to increase the design freedom of metasurfaces," J. Phys. D **54**, 135001 (2021).

66. Z. Shi, A. Y. Zhu, Z. Li, Y. Huang, W. Chen, C. Qiu, and F. Capasso, "Continuous angle-tunable birefringence with freeform metasurfaces for arbitrary polarization conversion," Sci. Adv. **6**, eaba3367 (2020).

67. M. Akbari, F. Samadi, A. Sebak, and T. A. Denidni, "Superbroadband diffuse wave scattering based on coding metasurfaces: polarization conversion metasurfaces," IEEE Antennas Propag. Mag. **61**, 40–52 (2019).

68. Q. Ma, G. Bai, H. Jing, C. Yang, L. Li, and T. J. Cui, "Smart metasurface with self-adaptively reprogrammable functions," Light Sci. Appl. **8**, 98 (2019).

69. H. Wang, Y. Jing, Y. Li, L. Huang, M. Feng, Q. Yuan, J. Wang, J. Zhang, and S. Qu, "Spin-selective corner reflector for retro-reflection and absorption by a circular dichroitic manner," Photon. Res. **9**, 726–733 (2021).

70. H. Xu, G. Hu, Y. Wang, C. Wang, M. Wang, S. Wang, Y. Huang, P. Genevet, W. Huang, and C. Qiu, "Polarization-insensitive 3D conformal-skin metasurface cloak," Light Sci. Appl. **10**, 75 (2021).

71. T. Shi, M. Tang, D. Yi, L. Jin, M. Li, J. Wang, and C. Qiu, "Near-omnidirectional broadband metamaterial absorber for TM-polarized wave based on radiation pattern synthesis," IEEE Trans. Antennas Propag. **70**, 420–429 (2021).

72. T. Shi, L. Jin, L. Han, M. Tang, H. Xu, and C. Qiu, "Dispersion-engineered, broadband, wide-angle, polarization-independent microwave metamaterial absorber," IEEE Trans. Antennas Propag. **69**, 229–238 (2020).